A Robust Inverse Design Solver for Controlling the Potential Aggressiveness of Cavitating Flow on Hydrofoil Cascades

Jeremy Nahon*[1] | Mehrdad Zangeneh[1] | Motohiko Nohmi[2] | Hiroyoshi Watanabe[2] | Akira Goto[2]

[1]Mechanical Engineering Department, University College London, London, United Kingdom
[2]Fluids Division, Ebara Corporation, Kanagawa, Japan

Correspondence
*Jeremy Nahon, Roberts Engineering Building, UCL, Torrington Place, London WC1E 7JE. Email: j.nahon@ucl.ac.uk

Abstract

This paper presents the development of a new inverse design algorithm capable of generating blade geometries for cavitating cascade flows. With this methodology, we demonstrate the controllability of the pressure distribution in and around the cavity and thereby provide a means to regulate the aggressiveness of blade cavitation phenomena. The solver poposed here uses the Tohoku-Ebara equation of state to model phase change, combined with bespoke preconditioning and multigrid methods designed to handle the system's ill conditioning and cope with the hypersonic flow regime of the mixture respectively. Blade geometries and the cavitating flow field are calculated simultaneously in a robust and efficient manner, with a blade loading that matches the target distribution. In this paper, the accuracy of the cavitating flow solver is first demonstrated for the NACA0015 hydrofoil case and associated experimental data. The inverse design procedure is then applied to a typical axial flow pump cascade: a new blade profile is generated with a topology that successfully reduces the gradient of the pressure jump at cavity closure.

KEYWORDS:
Inverse design; Hypersonic flow; Multi-phase flow; Finite volume; Phase Change; Explicit method; Validation

List of Symbols

α	Volume fraction or blade surface	
α_{nuc}	Vapour volume fraction at nucleation for the ZGB cavitation model, $\alpha_{nuc} = 5 \times 10^{-4}$ m	
β	Inflow angle	$^\circ$
$\boldsymbol{F}$	Convective flux vector	
$\boldsymbol{I}$	Grid to grid mapping operator	
$\boldsymbol{Q}$	Primitive variable vector	
$\boldsymbol{R}$	Residual vector in finite volume formulation	
Δp	Blade pressure loading	Pa
Δt	Discrete time step	s
$\dot{m}$	Mass flow rate	kg m^{-3} s^{-1}
Γ	Preconditioning matrix	
γ	Water vapour mass fraction	
κ	Multigrid shock weighting coefficients	
λ	Eigenvalues of linearised equations	
Ω	Rotational speed of pump/turbine or volume of control cell	rad s^{-1} or m^3

This article has been accepted for publication and undergone full peer review but has not been through the copyediting, typesetting, pagination and proofreading process which may lead to differences between this version and the Version of Record. Please cite this article as doi: 10.1002/fld.4974

ρ	Density or mixture density for homogeneous cavitating flow	$kg\,m^{-3}$
ρ_v	Saturation vapour density at 20 °C, $\rho_v = 0.0173$	$kg\,m^{-3}$
σ	Cavitation number	
Θ	Propagation parameter in preconditioning procedure	
ε	Turbulent dissipation rate	
ε, η	Curvilinear set of coordinates	
ζ	Angle of curvilinear axis ε	
c	Speed of sound	$m\,s^{-1}$
C^v, C^c	Vaporisation and condensation coefficients for the ZGB cavitation model, $C^v = 50$ and $C^v = 0.01$	
C_p	Pressure coefficient	
$chord$	Axial chord length	m
f	Camber line	
K	Liquid constant in the Tammann equation for liquid water, $K = 472.3$	$m^2\,s^{-2}\,K^{-2}$
k	Turbulent kinetic energy	J
M	Mach number	
p	Absolute static pressure	Pa
p_c	Critical pressure in the Tammann equation for liquid water, $p_c = 1.945 \times 10^9$	Pa
p_v	Saturation vapour pressure at 20 °C, $p_v = 2339.2$	Pa
R	Ideal gas constant, $R_v = 461$ and $R_g = 287.1$	$J\,kg^{-1}\,K^{-1}$
R_B	Bubble radius at nucleation for the ZGB cavitation model, $R_B = 1 \times 10^{-6}$ m	
T	Temperature or blade tangential thickness	K or m
T_c	Critical temperature in the Tammann equation for liquid water, $T_c = 3.837 \times 10^3$	K
u, v	Flow velocity vector	$m\,s^{-1}$
V	Contravariant velocity	$m\,s^{-1}$
x, y	Two-dimensional coordinate system	m
Y	Mass fraction of air in mixture, $Y = 1 \times 10^{-5}$	

Subscripts/Superscripts

∞	Upstream free stream values
$\overline{()}$	Upwind smoothed residuals
$\pm$	Pressure surface or suction surface
$\tilde{()}$	Shock weighted residuals
ε, η	Component indices in curvilinear coordinates
g	Non-condensable gas
$h, 2h$	Multigrid layer index
i, j	Coordinate indices
l	Liquid phase
R, P	Restriction or prolongation indices
v	Water vapour phase
x, y	Component indices in 2D coordinates

Abbreviations

2D	Two-dimensional formulation
CFD	Computational Fluid Dynamics
CFL	Courant-Friedrichs-Lewy number
EOS	Equation of State
LE	Leading Edge
ODE	Ordinary Differential Equation
RANS	Reynolds Averaged Navier-Stokes equations
RMS	Root Mean Square residuals
SLAU	Simple low dissipation advection upstream method
TE	Trailing Edge
ZGB	Zwart-Gerber-Belamri cavitation model

1 | INTRODUCTION

With the miniaturisation of pump systems, cavitation aggressiveness is intensified. Erosion, caused by the repeated collapse of gaseous bubbles in proximity to solid surfaces, occurs at accelerated rates that dramatically downgrade the life expectancy of rotating parts and cancel out the gains in performance delivered by the reduced size stage. As a result, the compacting strategy, meant to reduce cost and improve efficiency, breaks down for liquid flows.

To make the miniaturisation trend viable, new solutions are needed to dampen the aggressiveness of cavitation. Current provisions against cavitation in impellers or runners follow empirical recommendations, e.g. reducing inlet blade angle and diameter, *L* shaped loading.[1] The issue with this type of approach is that it is only concerned with delaying the onset of cavitation. Until now, only limited efforts have been invested in understanding the effect of geometry on cavity aggressiveness. The studied strategies suffer from either unconventional design additions, e.g. hole punching,[2] limited exploration and control of the geometry space,[3] or only address the lift and drag performance changes under cavitating conditions.[4]

Experimental research on hydraulic machinery has shown that the intensity of cavitation erosion is driven by the characteristics of the cavity structure. Shape, unsteadiness and noise notably play crucial parts.[5,6,7,8] A distinctive feature of attached blade cavities is the large pressure jump at closure. It is caused by the sudden deceleration of liquid as the wall effect created by the vapour sheet vanishes. Here, it is postulated that the closure shock is a determining factor in the aggressiveness of cavitation. It is, indeed, understood that erosion is caused by high pressure shock waves emanating from collapsing bubbles and liquid micro-jets impinging onto solid surfaces.[9] It has been shown that these mechanisms are directly driven by the difference between ambient and bubble pressure.[10] So, a direct correlation exists between the amplitude of the pressure jump and potential erosiveness of cavitation.

Here, we develop a novel design methodology that enables control over the pressure profile in and around the cavity. With this strategy, the ultimate objective is to be able to design blades that reduce the aggressiveness of cavitation by minimising the amplitude of the pressure jump. The approach is based on the inverse design technique which provides the means to generate blade profiles that comply to prescribed flow features. It has already been applied with success to suppress shocks in transonic compressors, eliminate secondary flows and delay cavitation breakdown using single phase flow models.[11,12,13] The method has, however, never been applied to cavitating or multiphase flows, or been used to tackle erosion.

Our methodology addresses cavitation for stationary hydrofoil cascades. This configuration constitutes a two-dimensional transformation of the three-dimensional axial flow impeller problem. This, however, does not downgrade the relevance of our strategy given that, in propellers and pumps, the streamwise variations are far greater than those occurring in the spanwise direction.

We also choose to omit viscous terms from the flow formulation. This is justified by considering the mechanism at the origin of sheet cavity instability. Indeed, it is the imbalance in pressure around the cavity closure point that leads to the formation of the re-entrant jet. This chain of events is governed solely by inertial effects such that viscous contributions can be neglected for cavitation instability and erosion studies.[14,15,16]

Furthermore, with inverse design, it is time independent solutions that are computed such that the inherent unsteadiness of sheet cavity is not captured. Nevertheless, our strategy is based on the potential cavitation energy formulation which is dependent on the surrounding liquid pressure rather than internal cavity characteristics,[10] meaning that the approach presented here remains valid and works by softening the pressure gradient over the region that contains the fluctuations of the cavity closure point.

The present paper details the development of the inverse design solver for cavitating cascades and provides proof of its effectiveness for closure shock control. The paper is split in two parts. The first is concerned with the development of the CFD solver for cavitating flow. It presents the inviscid governing equations, the selected cavitation formulation and its derivation, as well as crucial numerical techniques with particular emphasis placed on the tailored preconditioning and multigrid techniques responsible for enhancing the computational effectiveness of the code. The performance of the solver is validated against commercial CFD programs and experimental results for the well-known NACA0015 2D cavitating hydrofoil. In the second part, we detail the numerical formulation of the blade geometry problem and the schemes appended to the CFD solver to arrive at the target geometry. The inverse methodology is tested by carrying out a design experiment in cavitating conditions with the imposition that the closure jump be smoothed out and assessing the performance of the new geometry.

2 | CAVITATING FLOW SOLVER

2.1 | Governing equations and solution procedure

For the prediction of cavitating flow we follow the homogeneous mixture approach, wherein the liquid and vapour are formulated as a single phase of varying density, as is commonly done for flows around hydrofoils, impellers, propellers, runners or through nozzles. Homogeneous models branch out into two categories: void fraction transport equation methods and pressure-density coupling methods. The former append the Navier-Stokes governing system with a transport equation designed to capture the convection of vapour, as well as the condensation and vaporisation rates. Models differ in their treatment of the condensation and vaporisation source terms: derived from Rayleigh-Plesset bubble growth[17,18,19,15] or from bulk cavity growth.[20,21] In contrast, pressure-density coupling methods introduce a state law to close the governing system. The mixture state law is derived by amalgamating the pure liquid water state, the pure vapour state and the transition state. The pressure-density characteristics of the transition state are determined either artificially, e.g. sinusoidal,[22] by assuming local volume and mass equilibrium,[23,24] or by taking into account the temperature equilibrium[14,15] of the pure states within the mixture.

Here, we have opted for the pressure-density coupling approach because of its inclusion of liquid compressibility and higher accuracy for steady state cases[25] and have assumed isothermal conditions. The flow is governed by the Euler equations as it was shown by Schmidt et al.[26] that the effects of viscosity on cavitation aggressiveness are negligible. In the conservative preconditioned finite volume form

$$\mathbf{\Gamma}\frac{\partial}{\partial t}\int_{\Omega}\boldsymbol{Q}d\Omega+\oint_{\partial\Omega}\boldsymbol{F}dS=0 \tag{1}$$

with $\boldsymbol{Q}=[p \quad u \quad v]^T$ being the primitive variable set, Γ the preconditioning matrix, Ω and $\delta\Omega$ the finite cell volume and bounding area, and

$$\boldsymbol{F}=\begin{pmatrix}\rho V\\ \rho V u+pn_x\\ \rho V v+pn_y\end{pmatrix} \tag{2}$$

the inviscid flux vector expressed in terms of the contravariant velocity at the face $V=un_x+vn_y$ with n_x, n_y being the components of the unit normal vector at cell faces. Fluxes are computed using the Simple Low dissipation Advection Upstream (SLAU) flux vector splitting method[27] with high-order MUSCL reconstruction. It was tested against competing fluxing schemes and produced the sharpest solution.

The time derivative preconditioning matrix $\mathbf{\Gamma}$ is of the form

$$\Gamma=\begin{pmatrix}\Theta & 0 & 0\\ \Theta u & \rho & 0\\ \Theta v & 0 & \rho\end{pmatrix} \tag{3}$$

where Θ is a flow dependent parameter used to control propagation speeds. This is particularly important for cavitating flow, where high sound speed liquid and low sound speed gas lead to a large condition number, i.e. ratio of maximum over minimum eigenvalues, which downgrades the rate of convergence ant the accuracy of the numerical approximation. The change of update variable from conservative to primitive is advantageous because $\boldsymbol{Q}$ is more practical for building higher order reconstruction, and using pressure in the continuity equation means that the acoustic waves can be isolated.[28]

The novelty in the definition of the preconditioning matrix $\mathbf{\Gamma}$ and parameter Θ comes from the combination of the methods proposed by Weiss & Smith[28] and Turkel.[29] In Weiss & Smith,[28] the authors derive an approach compatible with the flux (finite volume) formulation of the flow equations and with arbitrary equations of state. The resulting matrix is identical in form to matrix $\mathbf{\Gamma}$ used in our implementation (see Equation (3)) except for the energy conservation equation which is decoupled and eliminated here. The weakness of the Weiss & Smith[28] approach is that, to define Θ, the authors get rid of the directional dependency of the flux vector $\boldsymbol{F}$ and assume that the advection velocity is given by the local velocity module $\|v\|=\sqrt{u^2+v^2}$. In this manner, a generalised form of the eigenvalues of the preconditioned flux jacobian is deduced in a straightforward manner but at the cost of downgrading multidimensional stability. By contrast, Turkel[29] lays out an approach which seeks to derive and optimise the eigenvalues of the true two-dimensional system. To that end, a set of curvilinear coordinates $\varepsilon=\varepsilon(x,y)$ and $\eta=\eta(x,y)$ is introduced to provide a generalised splitting of the horizontal and vertical flux contributions independent of grid topology.

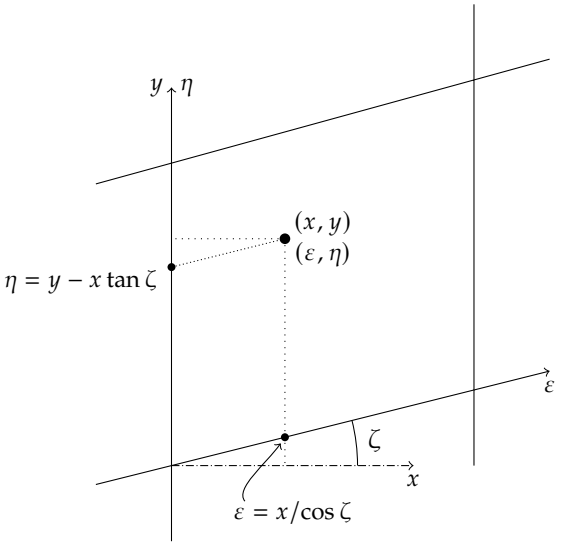

FIGURE 1 Cartesian to curvilinear transformation for the selected grid topology. The direction ζ of the curvilinear axis ε can be different at the south and north cell faces. To get a uniform cell transformation ζ is the arithmetic average of the two.

For our solver, we adopt a similar methodology and map our H-grid configuration (see Figure 1), expressed in (x, y) absolute coordinates onto the (ε, η) set

$$\begin{pmatrix}\varepsilon\\ \eta\end{pmatrix} = \begin{pmatrix}\frac{1}{\cos\zeta} & 0\\ -\tan\zeta & 1\end{pmatrix}\begin{pmatrix}x\\ y\end{pmatrix} \quad \text{and} \quad \begin{pmatrix}x\\ y\end{pmatrix} = \begin{pmatrix}\cos\zeta & 0\\ \sin\zeta & 1\end{pmatrix}\begin{pmatrix}\varepsilon\\ \eta\end{pmatrix} \tag{4}$$

Following Turkel,[29] the convective flux vectors in curvilinear space are converted into their Jacobian form and multiplied by the inverse of the preconditioning matrix such that the differential system looks like the canonical hyperbolic equation. By transforming the field into Fourier space, Jacobian flux matrices in each direction are concatenated into a single entity from which the true two-dimensional eigenvalues are extracted:

$$\begin{aligned}\lambda_0 &= \|v\|\\ \lambda_\pm &= \frac{1}{2}\left(\left(1+\frac{1}{\Theta c^2}\right)\|v\| \pm \sqrt{\left(1+\frac{1}{\Theta c^2}\right)^2\|v\|^2 + 4\left(2\left(1+|\sin\zeta|\right) - \frac{\|v\|^2}{c^2}\right)\frac{1}{\Theta}}\right)\end{aligned} \tag{5}$$

Parameter c represents the speed of sound and the term $2\left(1+|\sin\zeta|\right)$, specific to the topology used here (see Figure 1), is equal to the generalised expression $x_\varepsilon^2 + x_\eta^2 + y_\varepsilon^2 + y_\eta^2 + 2|x_\varepsilon x_\eta + y_\varepsilon y_\eta|$. The value for Θ is determined by minimising the ratio between the largest and smallest eigenvalues. Knowing that for low speed flows, $\|v\|^2/c^2 \ll 1$ and $1/(\Theta c^2) \ll 1$ it transpires that with

$$\Theta = \frac{1+|\sin\zeta|}{\|v\|^2} \tag{6}$$

the difference between eigenvalues is smallest. With this definition of Θ, the propagation speeds are scaled by a mesh topology weighted function of local fluid velocity and the preconditioning performs substantially better than the geometry agnostic version of Weiss & Smith.[28]

As usual for preconditioned flows, the value for Θ is bounded at low speeds so that any singularity is avoided and at high speeds to recover the well conditioned original system. Experience has shown that using the minimum Mach number, M_{min}, within the flow field as a global lower bound produces smooth and robust convergence such that

$$\frac{1}{\Theta} = \begin{cases} M_{min}^2 c^2 & \text{if } \|v\| < M_{min} c\\ \dfrac{\|v\|^2}{1+|\sin\zeta|} & \text{if } M_{min} c < \|v\| < c\\ c^2 & \text{if } c < \|v\| \end{cases} \tag{7}$$

The steady state solution is arrived at through explicit multistage time marching with coefficients given by Tai et al.[30] The local cell time step is

$$\Delta t = \frac{CFL\Delta_{min}}{\lambda^{+}} \tag{8}$$

where λ_{+} corresponds to the largest eigenvalue (see Equation (5)). The geometric parameter Δ_{min} is the cell minimum edge length and the CFL number is equal to 2.0. It is often argued that implicit schemes provide faster convergence and improved robustness owing to the independence of the relaxation on flow properties. In the author's experience, however, preserving the pseudo-time dependent formulation can serve to indicate the presence of unsteady and cyclical effects when residuals fail to drop, and, furthermore, the computational efficiency issue brought about by the boundedness of the pseudo-time step can be entirely compensated by implementing effective acceleration routines. These include time derivative preconditioning, multi-stage time stepping and multigrid (see Paragraph 2.3).

2.2 | Equation of State Model for Cavitating Flow

The pressure-density state law closing our governing equations is the *Tohoku-Ebara* equation of state.[24] It is an enhancement of the law proposed by Iga et al.[31] which is derived by blending two independent equations of state for the liquid and vapour phases: the Tumlirz-Tammann-Tait equation[32] and the ideal gas equation respectively. Using the definition of density for a homogeneous mixture $\rho = (1-\alpha)\,\rho_l + \alpha\rho_v$ – with α being the volume fraction, l and v subscripts for liquid and vapour respectively – and assuming local equilibrium, i.e. for pressure $p = p_l = p_v$ and temperature $T = T_l = T_v$, then both equations can be combined into

$$\rho = \frac{p(p+p_c)}{K(1-\gamma)p(T+T_c) + R_v\gamma(p+p_c)T} \tag{9}$$

Here, K is the liquid constant taken from the Tumlirz-Tammann-Tait equation, p_c and T_c are the critical pressure and temperature constants also from the Tumlirz-Tammann-Tait equation, R_v is the ideal gas constant for vapour and γ is the vapour mass fraction at nucleation. The values for these parameters are: $K = 472.3\,\mathrm{m\,s^{-2}\,K^{-2}}$, $p_c = 1.945\times10^{9}\,\mathrm{Pa}$, $T_c = 3.837\times10^{3}\,\mathrm{K}$, $R_v = 461\,\mathrm{J\,kg^{-1}\,K^{-1}}$, and $\gamma = 1\times10^{-5}$.

Nohmi et al.[24] improved the model by acknowledging the presence of entrained air in the liquid. In the gaseous phase, the pressure is therefore no longer given by the ideal gas equation for a single species but by

$$p = \rho\left(Y R_a + (1-Y)\,R_v\right)T \tag{10}$$

where Y is the mass fraction of air in the mixture, $R_a = 287.1$ J/kilogram /K and R_v are the ideal gas constants for air and vapour respectively. Substituting the new ideal gas law (equation (10)) and using the definition $1-\alpha = \frac{\rho}{\rho_l}\left(1 - Y - \frac{\rho_v}{\rho_g}Y\right)$ yields the Tohoku-Ebara mixture state law

$$\rho = \begin{cases} \dfrac{(p+p_c)(p-p_v)}{(1-Y)(p-p_v)K(T+T_c) - Y\rho_v K(T+T_c)R_aT + Y(p+p_c)R_aT} & \text{if } p > p_v \\ \dfrac{p}{(Y R_a + (1-Y)R_v)T} & \text{otherwise} \end{cases} \tag{11}$$

Below the vapour pressure p_v, the fluid obeys the ideal gas law for the air and vapour gas mixture. For the studied cases, temperature is assumed constant at $T = 293.15\,\mathrm{k}$ and the corresponding saturation vapour pressure is $p_v = 2339.2\,\mathrm{Pa}$. The amount of free stream nuclei is incorporated into the mixture mass fraction of air, which is given a value of $Y = 1\times10^{-5}$.

For the speed of sound of the cavitating mixture, one applies the formal definition for continuous media i.e. $c^2 = \partial p/\partial\rho$. Owing to the full dependency of density on pressure and vice-versa, we write

$$c^2 = \frac{\partial p}{\partial \rho} = \left[\frac{d\rho}{dp}\right]^{-1} \tag{12}$$

Numerically, a value for the speed of sound is easily computed by isolating the numerators and denominators in equation (11).

2.3 | Multigrid for Cavitating Flow

Here, we propose a bespoke Full Approximation Storage multigrid architecture designed to cope with the difficulties of our studied medium. Indeed, the large pressure/density jumps and extensive range in flow regime ($M < 0.1$ in liquid, $M > 10$ in cavity) that characterise the Tohoku-Ebara cavitating flow are smeared when transferred using central restriction or prolongation operators, leading to erroneous propagation of information and halted convergence.

The approaches chosen to remedy the aforementioned issues take inspiration from multigrid techniques for hypersonic flow problems. These introduce upwinding attributes into multigrid operators. Two procedures in particular have substantial positive effects:

- the upwinded residual smoothing technique laid out by Grasso & Marini[33] or Blazek et al.,[34]
- the Radespiel & Swanson[35] shock weighting operator.

The former, upwinded residual smoothing technique, relies on the same mechanism as the central residual smoothing approach i.e. enhancing the high frequency damping properties of the explicit scheme. The difference being that the smoothing coefficients are switched on or off according to the local propagation speed and direction. Here, we have opted for a straightforward implementation based on Mach number values. Reducing the discretised Euler equations to the generalised linear form

$$\boldsymbol{R}_h(\boldsymbol{Q}_h) = 0 \tag{13}$$

where $\boldsymbol{R}_h$ is the residual vector and index h indicates the grid resolution ($2h$, $4h$, $8h$ for coarser levels) the smoothing operation, in one dimension, is given by

$$\overline{\boldsymbol{R}}_i = [1 + \epsilon(a_i\Delta_+ - b_i\Delta_-)]\boldsymbol{R}_i \tag{14}$$

where Δ_+ and Δ_- correspond to the forward and backward (first order) finite difference operators, $\epsilon = 0.3$ is the smoothing coefficient, and index i represents a single finite volume cell. Upwinding is taken into account by coefficients a_i and b_i, defined such that

$$\begin{aligned} a_i = 0 \quad b_i = 1 \quad \text{if} \quad M_i > 1 \\ a_i = 1 \quad b_i = 0 \quad \text{if} \quad M_i < -1 \\ a_i = 1 \quad b_i = 1 \quad \text{if} \quad |M_i| \leq 1 \end{aligned} \tag{15}$$

where M is the local contravariant Mach number, $M = V/c$, dependent on the smoothing direction. For two-dimensional flow, each direction is considered independently. In the present multigrid implementation, the upwind smoothing procedure is carried out within the *prolongation* step only and applied to the coarse grid correction vector $\boldsymbol{\delta Q}_{2h} = \left(\boldsymbol{Q}^m_{2h} - \boldsymbol{Q}^{(0)}_{2h}\right)$.

The latter shock weighting procedure locates supersonic shocks by evaluating the change in pressure across neighbour cells. Physically, information cannot propagate through shocks in the upstream direction. However, with conventional grid transfer operators, there is no safeguard against the averaging of cells or application of the same coarse grid correction on different sides of a shock. To counteract these issues, the method introduces a damping procedure of the form

$$\tilde{\boldsymbol{R}}_i = \max(1 - \varepsilon, 0)\boldsymbol{R}_i \tag{16}$$

with

$$\varepsilon = \kappa_{R/P} \max(\nu_{i-1}, \nu_i, \nu_{i+1}) \tag{17}$$

and

$$\nu_i = \left| \frac{p_{i-1} - 2p_i + p_{i+1}}{p_{i-1} + 2p_i + p_{i+1}} \right| \tag{18}$$

$\kappa_{R/P}$ being a tunable parameter applied to either the restriction (index R) or prolongation (index P) that can vary with the coarseness and convergence levels. The shock weighting method is included in both restriction and prolongation steps, and therefore, takes on either the residual $\boldsymbol{R}_i$ or correction $\boldsymbol{\delta Q_{2h}}$ as its RHS term.

In the implementation presented here, the search for shocks and ensuing weighting is applied in the streamwise direction only to cut down computational load. For the prolongation procedure, the value for κ_P is set at $\kappa_p = 2.1$ throughout the multigrid cycle. For the restriction operator, it was found that the shock weighting strategy is only required when mapping from h (finest) to $2h$. So parameter κ_R is switched on or off following

$$\kappa_R = \begin{cases} 2.1 & \text{if } h \to 2h \\ 0 & \text{otherwise} \end{cases} \tag{19}$$

With these two techniques, the amount of information passed up and down the grid levels is controlled in sensitive high pressure gradient zones. In that region, most of the numerical work is relinquished to the fine grid. This increases the computational cost but the limited size of the sensitive region means that the convergence gains are comparable to those obtained for non-cavitating homogeneous cases. The steps that constitute the enhanced prolongation and restriction operations are detailed in Table 1 .

TABLE 1 Algorithmic operations carried out by the restriction and prolongation routines.

Grid Level	Algorithmic Operation	Expression
	Restriction	
h	Evaluate fine grid (preconditioned) residuals.	$\boldsymbol{R}_h = \Gamma_h^{-1}\boldsymbol{R}(\boldsymbol{Q}_h)$
h	Apply residual shock weighting.	$\tilde{\boldsymbol{R}}_h = \max(1-\varepsilon, 0)\boldsymbol{R}_h$
$h \rightarrow 2h$	Initialise coarse grid.	$\boldsymbol{Q}_{2h}^{(0)} = I_h^{2h}\boldsymbol{Q}_h^{(n)}$
$2h$	Calculate initial coarse grid residuals.	$\boldsymbol{R}_{2h}^{(0)} = \Gamma_{2h}^{-1}\boldsymbol{R}(\boldsymbol{Q}_{2h}^{(0)})$
$2h$	Assemble coarse grid forcing function.	$\boldsymbol{f}_{2h} = \boldsymbol{R}_{2h}^{(0)} - I_h^{2h}(\tilde{\boldsymbol{R}}_h - \boldsymbol{f}_h)$
	Prolongation	
$2h$	Evaluate coarse grid correction.	$\boldsymbol{\delta Q}_{2h} = \boldsymbol{Q}_{2h}^{(*)} - \boldsymbol{Q}_{2h}^{(0)}$
$2h$	Smooth correction using upwind strategy.	$\overline{\boldsymbol{\delta Q}}_{2h} = f(\epsilon, \boldsymbol{\delta Q}_{2h})$
$2h$	Apply shock weighting to correction.	$\tilde{\boldsymbol{\delta Q}}_{2h} = \max(1-\varepsilon, 0)\overline{\boldsymbol{\delta Q}}_{2h}$
$2h \rightarrow h$	Add correction to fine grid using bi-linear interpolation.	$\boldsymbol{Q}_h^{corrected} = \boldsymbol{Q}_h^{(n)} + I_{2h}^{h}\tilde{\boldsymbol{\delta Q}}_{2h}$

The implemented multigrid algorithm uses a 4-grid architecture and follows the sawtooth cycle with no iterations carried out before restriction and two carried out before prolongation (see Figure 2). At start-up, the solution is initialised on the coarsest grid and run for a finite number μ of iterations before being mapped onto the next fine level.

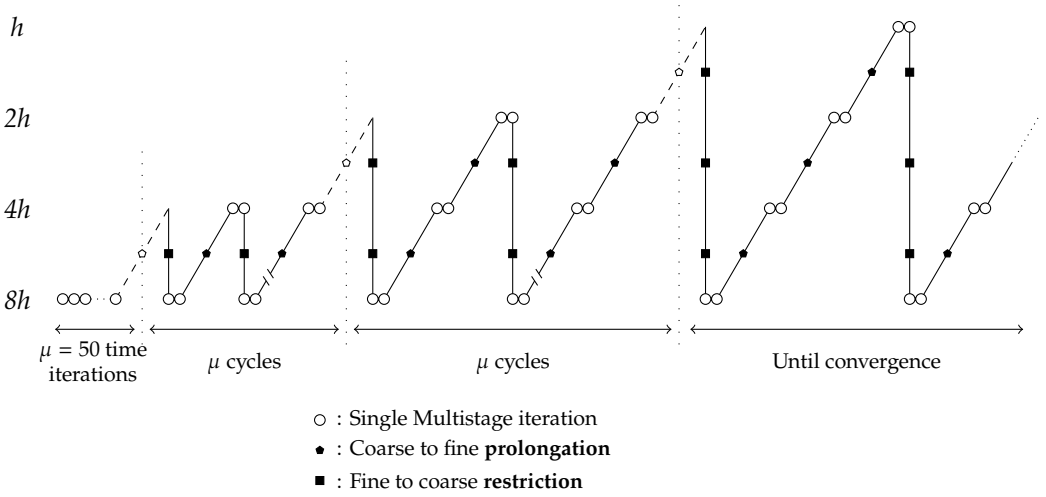

FIGURE 2 Four-grid FMG routine used to accelerate the calculation of steady state cavitating flow solutions. Note that no time-marching is carried out during restriction (from fine to coarse).

2.4 | Solver validation

To test the solver, we carry out an assessment of the NACA0015 hydrofoil under cavitating flow. The study follows the benchmark experimental analysis by Kato.[25] The 300 mm chord hydrofoil is placed in a 600 mm high water tunnel at an angle of attack of 8° and an inlet flow velocity of 8 m s^{-1}. The computational domain extends 5 chords upstream and downstream of the blade centre. We use a 6-block mesh topology divided along the centre streamline and at the leading and trailing edges (see Figure 3 for the full domain and mesh). For our analysis, the flow is inviscid so boundary layer refinement is not necessary. Upstream and downstream boundary conditions are adapted from the method of Choi & Merkle[36] for time-derivative preconditioned equations such that velocity magnitude and flow direction are imposed at the inlet and static pressure at the outlet. On top of the experimental data, the results are compared against the solution obtained using ANSYS Fluent with the Zwart-Gerber-Belamri cavitation model and the RANS $k-\epsilon$ approach with scalable wall functions for turbulence. The ZGB model parameters are those recommended by the authors in Zwart et al.,[18] i.e. $C^v = 50$, $C^c = 0.01$, $R_B = 1 \times 10^{-6}$ m and $\alpha_{nuc} = 5 \times 10^{-4}$. For this setup we construct a conventional C-block grid topology with appropriate boundary layer refinement ($y^+ \approx 30$).

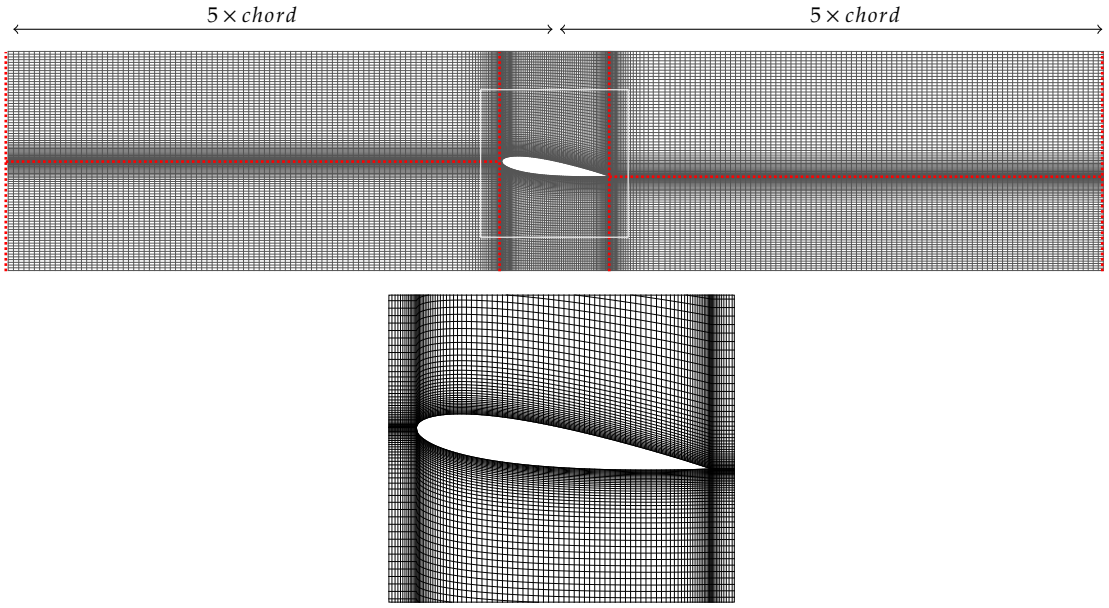

FIGURE 3 Mesh for the in-house run of the NACA0015 hydrofoil at $\sigma = 1.8$.

In Figure 4 , the C_p distributions around the blade are shown for flow at cavitation number $\sigma = 1.8$ with

$$\sigma = \frac{p_\infty - p_v}{\frac{1}{2}\rho_l v_\infty^2} \tag{20}$$

p_∞ and v_∞ being respectively the inlet free stream static pressure and velocity, and ρ_l liquid water density. We compare the results obtained from our in-house cavitating flow solver to the Fluent with ZGB modelling solution and to the experimental data from Kato.[25] There is an evident agreement between our computed results and the experimental measurements. As a matter of fact, the cavity closure position delivered by our solver ($x/chord = 0.3$) is far closer to the measured reference than the one computed using the ZGB model ($x/chord = 0.2$). This is due to the inherent compressibility of our medium brought about by the assumption of entrained non condensable gas which accelerates vaporisation as observed by Brennen.[9] The mismatch in C_p values on the suction side downstream of the cavity comes from the absence of viscous/RANS modelling in a region where boundary layer effects are strong. Figure 5 presents the cavities obtained from both solvers and confirms the size discrepancy of the vapour regions. It is interesting to note the gradual increase in volume fraction for the Tohoku-Ebara equation of state in lieu of the sharp jump produced by the ZGB model. This property enhances the cavity wall effect such that the Tohoku-Ebara closure jump presents a sharper gradient and larger amplitude. This more diffuse characterisation of blade cavitation

is more resemblant to industrial manifestations of the phenomenon wherein non-purified water tends to produce more bubbly vapour-liquid interfaces.

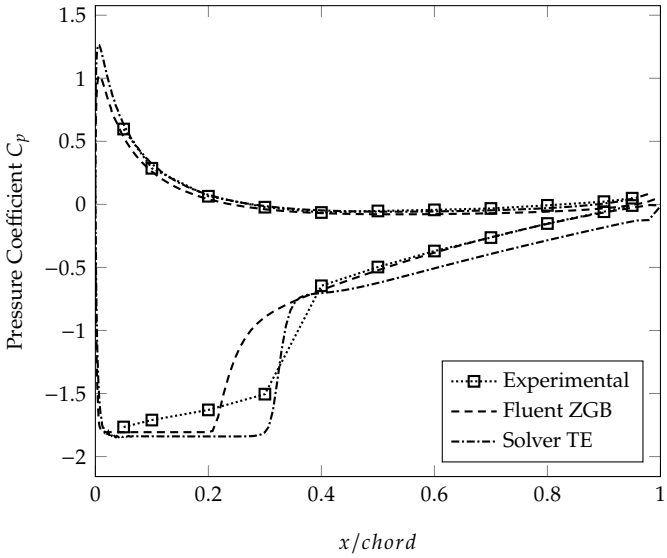

FIGURE 4 Comparison of measured and computed surface pressure distributions around the NACA0015 hydrofoil at $\sigma = 1.8$ ($v_\infty = 8\,\mathrm{m\,s^{-1}}$ and $\beta = 8°$). Experimental data from Kato.[25]

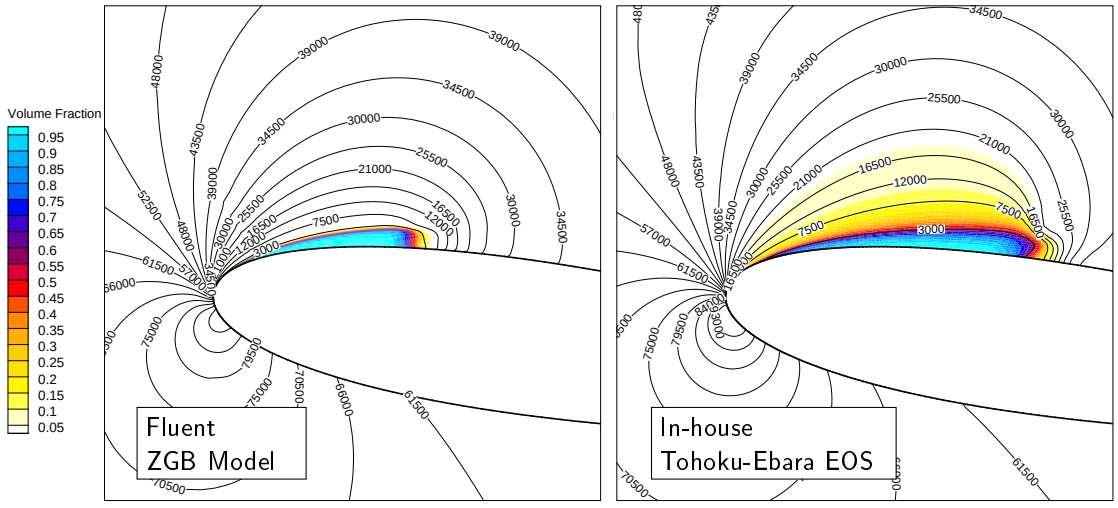

FIGURE 5 NACA0015 pressure and volume fraction contours at $\sigma = 1.8$ ($v_\infty = 8\,\mathrm{m\,s^{-1}}$ and $\beta = 8°$) computed by Fluent with the ZGB cavitation model (left) and by our in-house solver using the Tohoku-Ebara equation of state (right).

3 | INVERSE DESIGN PROCEDURE

Having demonstrated the reliability of the CFD part of our solver we now address the techniques used to treat the inverse design problem. Several strategies have been developed but many lack the robustness required for industrial design.[37,38,39] The issue is the absence of a formal mathematical definition for expressing the blade geometry. The implementation presented here follows the formulation given by Hawthorne et al.[40] The blade surfaces $\alpha^{\pm}$ (superscript + for the pressure side, superscript − for the suction side) are expressed in terms of the camber line $f(x)$ and tangential thickness distribution T:

$$\alpha^{\pm} =: y - (f(x) \pm T/2) = ns \tag{21}$$

where n is the blade number and s the pitch length. This definition carries the crucial advantage of ensuring a closed and non-intersecting blade geometry easily by maintaining a strictly positive thickness distribution and imposing $T = 0$ at the leading and trailing positions. The inverse design procedure is built such that the geometry modifications it brings about are applied to the camber line $f(x)$ while thickness T is kept constant. With this implementation, the design procedure relies on a single additional degree of freedom bestowed upon camber nodes which are allowed to move up and down in the tangential direction. The blade pressure and suction surfaces are bound together by the constant thickness imposition meaning that prescribing the flow quantities on each surface independently is not a feasible approach.

Instead, the technique laid out by Dang et al.,[41] which uses the pressure loading $\Delta p = p^{+} - p^{-}$ along the blade channel is adopted here. The stagnation point at the leading edge and Kutta condition at the trailing edge are constraints which are incorporated into the Δp loading by enforcing a zero value at these positions. In between that, the shape of the distribution is entirely free. Incidence is controlled through the leading edge gradient and the swirl difference across the channel, equivalent to the work output, is adjusted using the relation:

$$\int_{LE}^{TE} \Delta p \, dm \propto \dot{m} \left(\overline{V_y}^{TE} - \overline{V_y}^{LE} \right) \tag{22}$$

which implies that the integral of the difference in pressure across the blade, Δp, over the streamwise coordinate dm is proportional to the swirl change through the cascade channel, with $\overline{V_y}$ being the mass flow averaged pitchwise velocity calculated at the trailing and leading edges. In this numerical method, the new degree of freedom granted to the blade is balanced by the loading condition at the camber line such that, mathematically, the problem remains well posed.

3.1 | Acoustically Permeable Wall

At the blade surfaces, the solid wall is replaced by a permeable boundary condition allowing flow to pass through the surface. The pressure jump across the blade is enforced by setting the pressure at the top and bottom surfaces using

$$p^{n}_{\pm} = \langle p^{n} \rangle \pm \frac{\Delta p}{2} \tag{23}$$

where $\langle p^{n} \rangle = \frac{1}{2}(p^{n}_{+} + p^{n}_{-})$ is the average of the current computed pressure values at the suction and pressure sides.

In Dang et al.,[41] the authors propose two strategies for setting the flow state at the permeable boundary. The first is derived from the free slip condition formulation which provides an expression for the tangential velocity component at the permeable wall v^{*} in terms of the camber and thickness distributions. The axial velocity component u^{*} and the density ρ^{*} imposed on both sides are assumed equal to the average of the computed values $\langle u^{n} \rangle$ and $\langle \rho^{n} \rangle$. For the cavitating flow and cascade geometry studied here, it was found that, because of the large thickness and strong changes in density, this approach constitutes an excessively stringent boundary condition which prevents solution advancement.

The second strategy laid out in Dang et al.[41] originates from the work by Demeulenaere et al.[42] who consider that the information propagating through the interface is analogous to the ingoing or outgoing waves travelling from inflow or outflow boundaries. As such, the flow states assigned at the permeable wall are extracted from compatibility relations taken along the suction and pressure surfaces. Our implementation is similar in rationale to the latter as it acknowledges the propagating contribution generated by the boundary. However, its construction follows a different, more efficient approach wherein the surface pressure imposition (equation (23)) is passed into the computational domain through acoustic propagation exclusively. This means that the reflecting boundary used at free slip walls when solving the pure Euler equations can be employed with a slight but crucial modification: instead of assigning the outer pressure equal to the inner one, it takes on the value demanded by the loading prescription. The other flow variables retain the characteristics of the reflecting boundary i.e. mirror image for velocity and equal

density. The contribution from the outside of the wall is calculated, as with all internal cells, using the SLAU approximation for the flux through the face. By design, the flux contains a null convective part and a non-null acoustic (pressure) part which breaks the tangency condition on the inside of the wall in a manner consistent with the pressure loading prescribed by the designer.

The strategy presented here is advantageous for several reasons. First, its implementation is straightforward requiring only a simple modification of existing reflecting boundaries. Secondly, the imposition of the pressure loading unfolds gradually from the non-converged flow field without causing any sharp disturbances likely to damage computational stability. Finally, relying only on pressure makes the strategy compatible with the no-slip condition for future viscous and RANS flow calculations.

3.2 | Blade Update Algorithm

The changes in velocity direction at the wall induced by the imposed pressure are translated to geometry modifications by reformulating the free slip condition. At the blade surfaces, we write

$$\mathbf{V}^{\pm} \cdot \nabla \alpha^{\pm} = 0 \tag{24}$$

where $\mathbf{V} = (u, v) = \left(V_x, V_y\right)$ is the velocity vector at the wall. Equation (24) is rewritten by summing the tangency condition on both surfaces

$$\mathbf{V}^{+} \cdot \nabla \alpha^{+} + \mathbf{V}^{-} \cdot \nabla \alpha^{-} = 0. \tag{25}$$

By introducing the blade definition (21) into (25) and expanding we find that

$$\langle V_x \rangle \frac{\partial f}{\partial x} = \langle V_y \rangle - \frac{1}{4} \Delta V_x \frac{\partial T}{\partial x} \tag{26}$$

with

$$\langle () \rangle = \frac{1}{2} \left(()^{+} + ()^{-} \right) \qquad \Delta() = ()^{+} - ()^{-} \tag{27}$$

Equation (26) essentially constitutes the ordinary differential equation that relates velocity direction with camber. The new camber line f^{n+1} is obtained by integrating (26) numerically from a static seed point. In the current implementation, the latter is consistently placed at the leading edge. Blade updates are carried out after each multigrid cycle. The algorithmic workflow of the complete methodology is laid out in Figure 6 . As the solution advances, the gap between the pressure computed at the wall and the prescribed value decreases, as does the angle between the velocity vector and the gradually stabilising wall. The fluid computation and the design procedure being amalgamated into one single computational problem, no additional convergence control mechanisms are necessary other than the conventional RMS values for pressure and velocity.

4 | APPLICATION OF INVERSE DESIGN

For the inverse design experiment, the first step consists in defining the geometry of the Baseline case (Section 4.1) which serves as reference for flow performance and as the initialisation to the inverse design procedure. We then carry out the design in cavitating conditions (Section 4.2) and aim to generate a smoothed closure pressure jump using the presented inverse design algorithm. The success of the new geometry is assessed through CFD.

4.1 | Baseline Cascade

It is imperative that the baseline cascade presents flow characteristics, i.e. meridional velocity, swirl and static pressure, similar to those found in pump impellers. To meet this requirement, we design an arbitrary axial flow impeller with solidity ratio $chord/pitch = 1.5$ and extract the profile at the shroud to construct the 2D blade. The resulting geometry is shown in Figure 7 along with the mesh. We use a single structured H-block to discretise our domain, with parallel vertical grid lines to facilitate the re-meshing after each geometry update.

The operating conditions of the stationary cascade are determined by replicating the velocity triangle at the inlet and tip of the pump at design conditions. The 2D inflow velocity vector for the cascade therefore corresponds to the relative vector at the shroud with the circumferential component given by $U = R\Omega = 10.472\,\mathrm{m\,s^{-1}}$. The axial velocity remains unchanged at $V_x = 10\,\mathrm{m\,s^{-1}}$. For the cascade configuration, the boundary conditions are modified such that stagnation pressure and flow direction are imposed at inlet and mass flow, through back pressure feedback adjustment, is imposed at outlet. This allows for direct control over the cavitation number at the inlet and ensures the design condition velocity through the cascade.

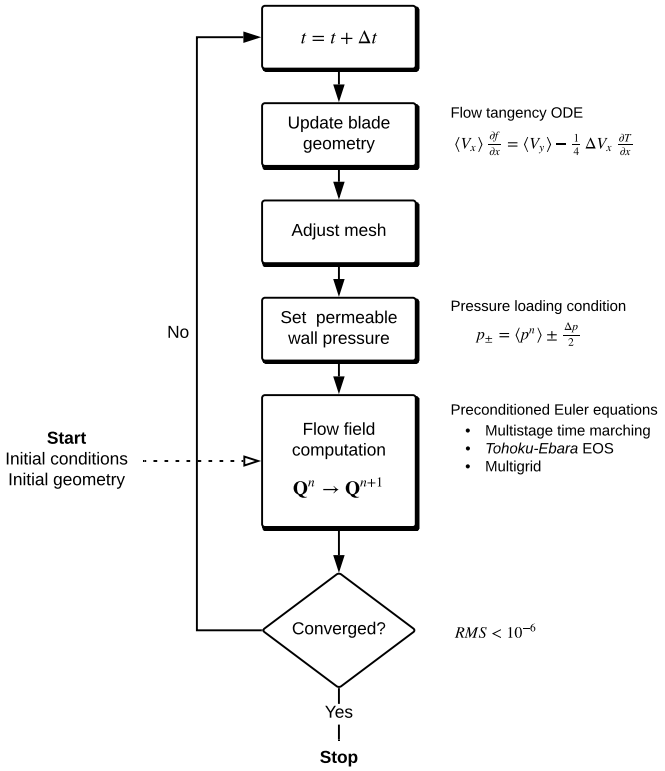

FIGURE 6 Algorithmic work-flow of the inverse design methodology for cavitating flow.

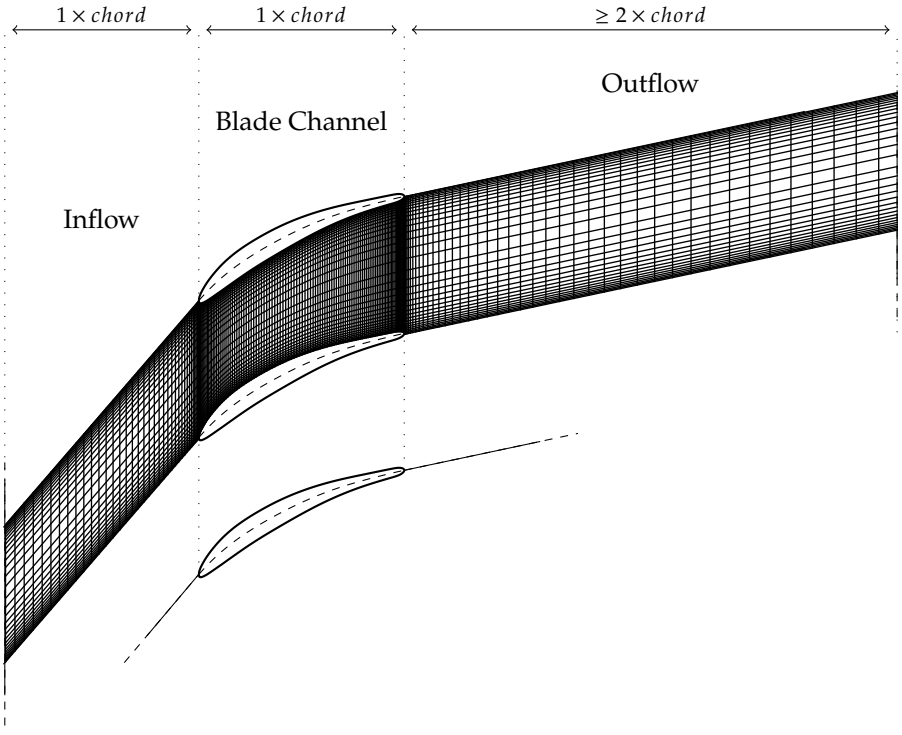

FIGURE 7 Discretisation of the cascade channel: an H-grid topology is used in conjunction with structured quadrilateral cells.

The blade pressure distribution obtained from our cavitating flow solver is shown in Figure 8 in both non-cavitating and cavitating conditions. As required, particular features of impeller flow are recovered: leading edge incidence is close to zero, increase in pressure through the channel. At low σ, cavitation is formed on the blade suction surface exclusively and the sharp closure shock is a clear feature of the flow.

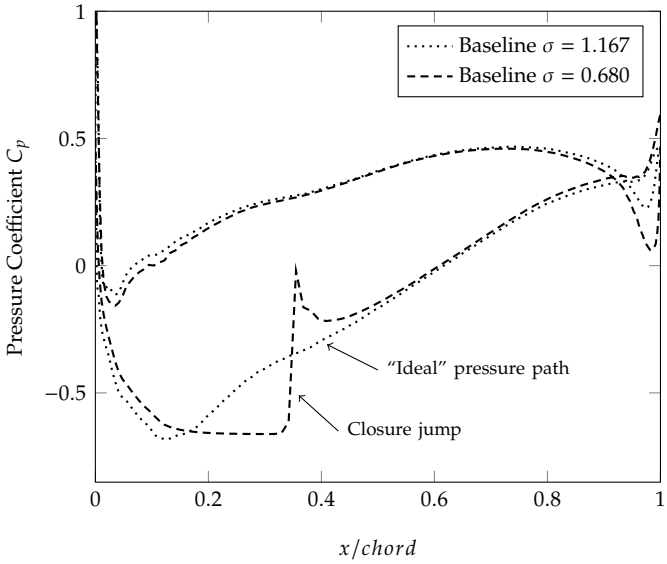

FIGURE 8 Surface pressures in non-cavitating ($\sigma = 1.167$) and cavitating ($\sigma = 0.68$) conditions for the Baseline case. Data computed by our in-house developed solver. When cavitation occurs, the pressure on the suction surface rejoins with the 'ideal" (non-cavitating) pressure downstream of the closure jump.

4.2 | Closure Pressure Jump Manipulation

The aim is to show that our methodology can control the profile of the cavity pressure jump and thereby reduce the aggressiveness of cavitation. To that end, we take the cavitating baseline loading and modify it in the closure region only. The rest of the profile remains unchanged (see Figure 9) in order to maintain the global performance of the cascade. The new distribution is used as input to the inverse design computation which is run at $\sigma = 0.68$ in the same velocity conditions (see equation (20) for the definition of σ).

Convergence is attained after a number of iterations similar to that of the purely analytical runs. The loading obtained at the end of the computation is shown in Figure 9 and overlaps well with the prescribed distribution. The only discrepancy is located at cavity closure where a small amplitude jump is found slightly upstream of the original closure location. Blade pressure under cavitating conditions shows a clearly smoothed post-cavitation recovery as was targeted when imposing the loading profile (see Figure 10). We also note that our new design shortens the axial length of the cavity ($x/chord = 0.35$ for baseline, $x/chord = 0.31$ for the new design). On the blade pressure side, a wavy pressure feature positioned at the same axial plane as the cavity closure is observed. This is due to the particular shape of the new design which presents a small scale kink at $x/chord \approx 0.3$ made visible when comparing the camber line angles (Figure 11). This non-standard feature is the principal product of the smoothed design concept and translates to a non monotonous pressure distribution on both sides of the blade (see the non-cavitating pressure distribution Figure 10).

The characteristic wavy distribution is essential in understanding how our design is able to smooth the closure jump. Indeed, when cavitation occurs, the pressure rise – caused by the sudden increase in throat cross section – connects p_v to the "ideal" non-cavitating pressure, see for example Figure 8 . With the improved geometry, the induced camber bending is such that, (i) the position of the second pressure minimum is superimposed on the cavity closure and (ii) the post-closure region is characterised by a low pressure gradient. As a result, the closure jump connects pressure levels that are only marginally separated. In effect,

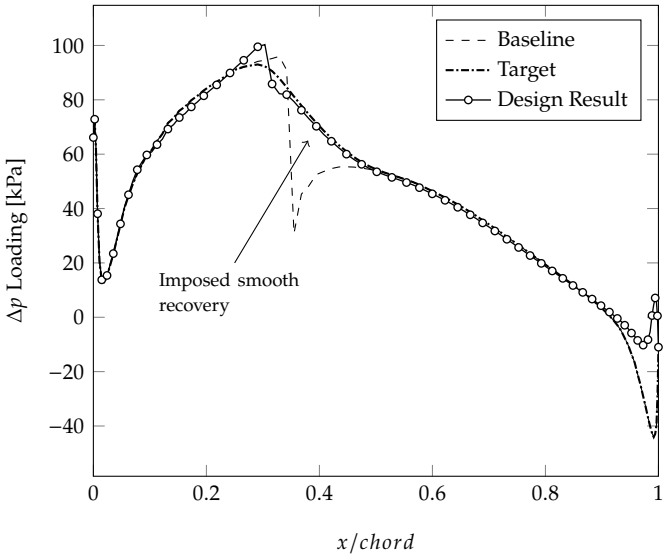

FIGURE 9 Comparison of Δp loading distributions for the baseline case, the target and the result obtained after the inverse design run.

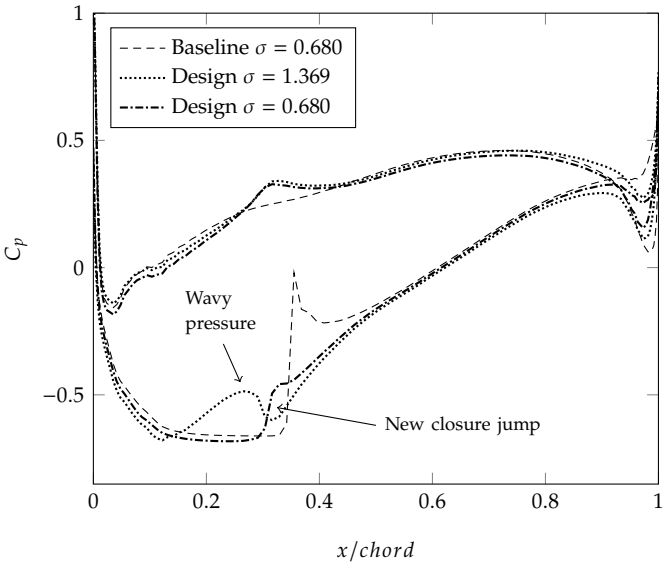

FIGURE 10 Blade pressure distributions for the baseline and design geometries at $\sigma = 0.68$ and $\sigma = 1.369$ (non-cavitating) for the design.

the amplitude of the shock is related to the difference between the first and second suction side pressure drops found for non-cavitating flow. The closer they are, the smaller the amplitude of the jump when cavitation does occur.

In terms of blade geometry, the most notable discrepancy is found at the cavity closure location in the form of a minor deviation from the original blade surfaces. At the trailing edge, the offset is produced by the inverse design algorithm compensating for the smoothed loading in the shock region. An important observation made here is the similarity in shape between the baseline and the designed blade (see Figure 12). The implication is that the hydrodynamic performance remains unadulterated and that, more importantly, the geometry presents no non-manufacturable features.

Comparison of the pressure and volume fraction contours for the Baseline and Design is presented in Figures 13 and 14 . For the Design case, we observe a shorter and thinner cavity length and, most notably, the absence of sharp pressure gradients.

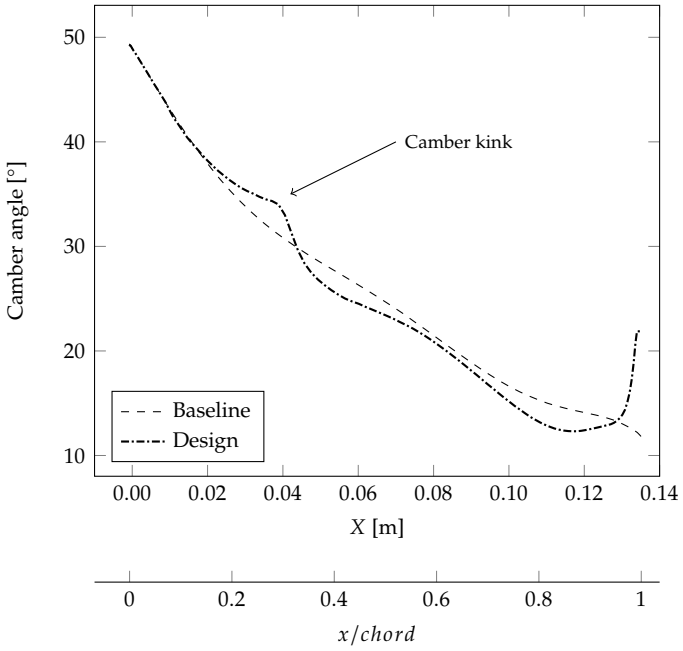

FIGURE 11 Camber line angles (from X axis). The camber kink for the new design is visible at $x/chord = 0.3$. From the leading edge to $x/chord \approx 0.1$ the blades are exactly identical.

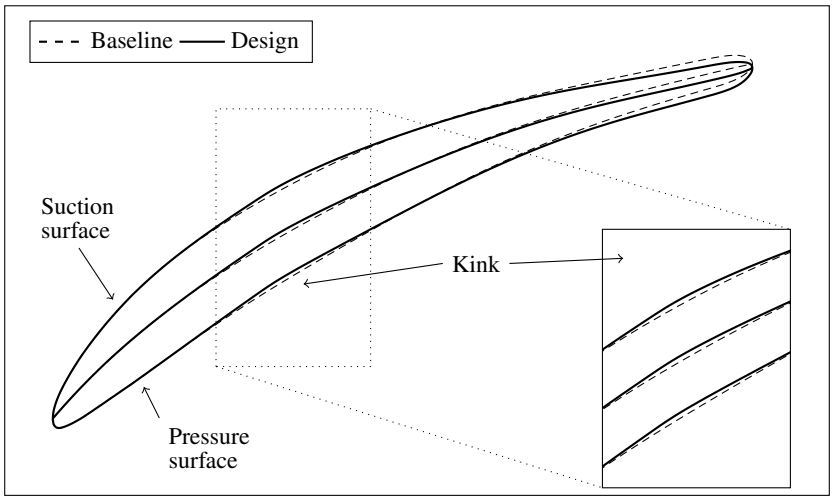

FIGURE 12 Comparison of full blade geometries. The effect of the loading modification on the shape is only perceptible in the kink region and at the trailing edge.

At these scales, the geometry bend is not noticeable. A characteristic of interest concerns the behaviour of pressure around the closure region. A sharp change of direction in the pressure contour from normal to parallel to the surface is observed. In Figure 14 , the close up view of the closure region indicates that the direction change emanates from the surface kink: the geometric discontinuity is essentially propagated into the flow field until diffused.

The Baseline and Design geometries are also analysed using Fluent with the ZGB model and RANS $k - \varepsilon$ turbulence with scalable wall functions in order to (i) provide solutions that take into account viscous and turbulent effects, (ii) confirm the smoothed shock profile using a competing cavitation model. Adequate meshes were generated with body fitted inflation layers (20 nodes and $y^+ < 30$). Pressure distributions for descending cavitation numbers are presented in Figure 15 . It was shown in Section 2.4 that the ZGB model tends to under-predict the onset of cavitation for 2D flows, hence the discrepancy in cavity

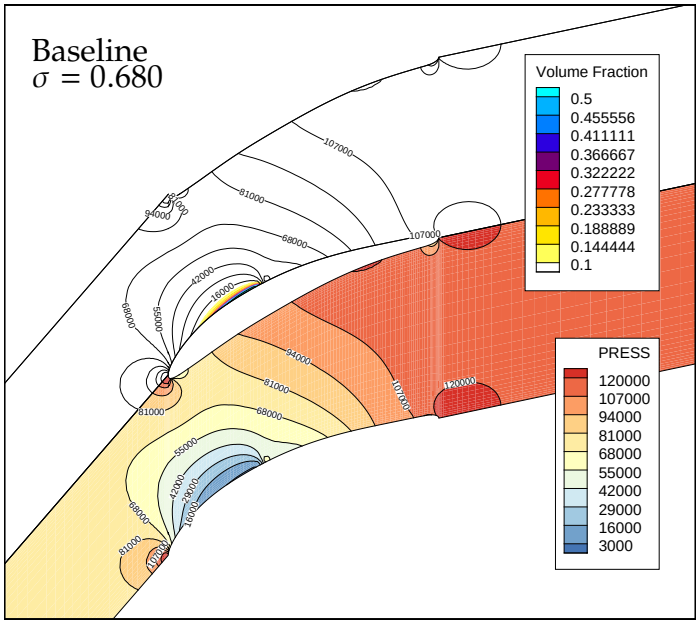

FIGURE 13 Pressure and volume fraction contours for the baseline case at $\sigma = 0.680$.

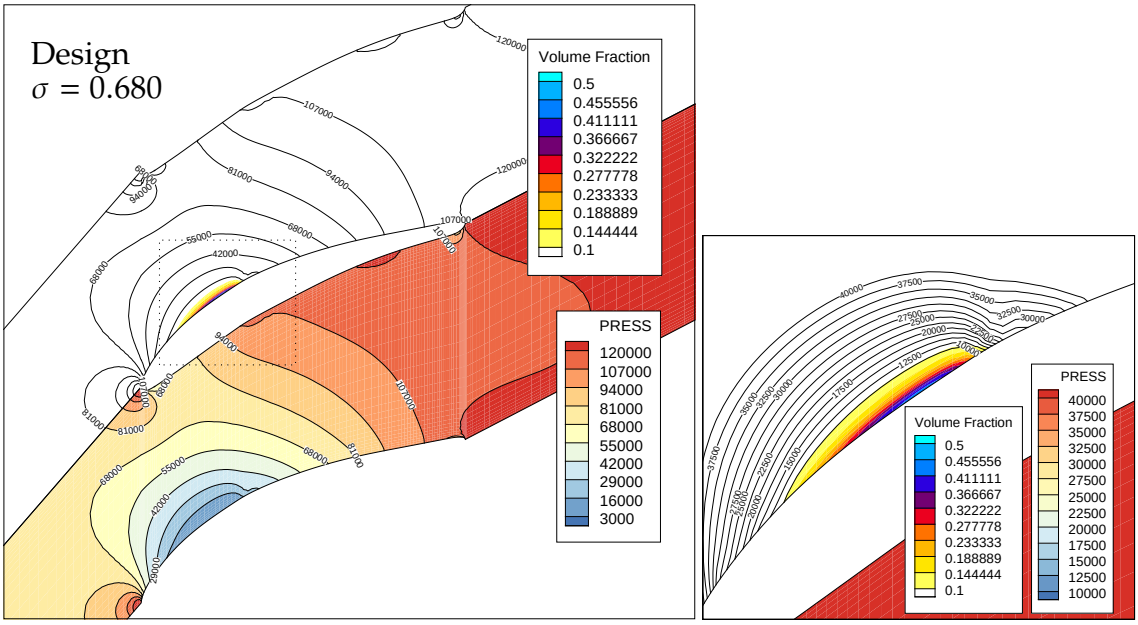

FIGURE 14 Pressure and volume fraction contours for the new design at $\sigma = 0.680$ with close-up on cavitating region.

length with the in-house solution at $\sigma = 0.680$ (se Figure 10). Regardless, Fluent results confirm the observations made earlier: the jump amplitude is consistently lower for the new design with a significant smoothing effect when closure is located at $x/chord \approx 0.35$ thanks to the wavy pressure distribution, and a general reduction in cavity length (see Figure 16).

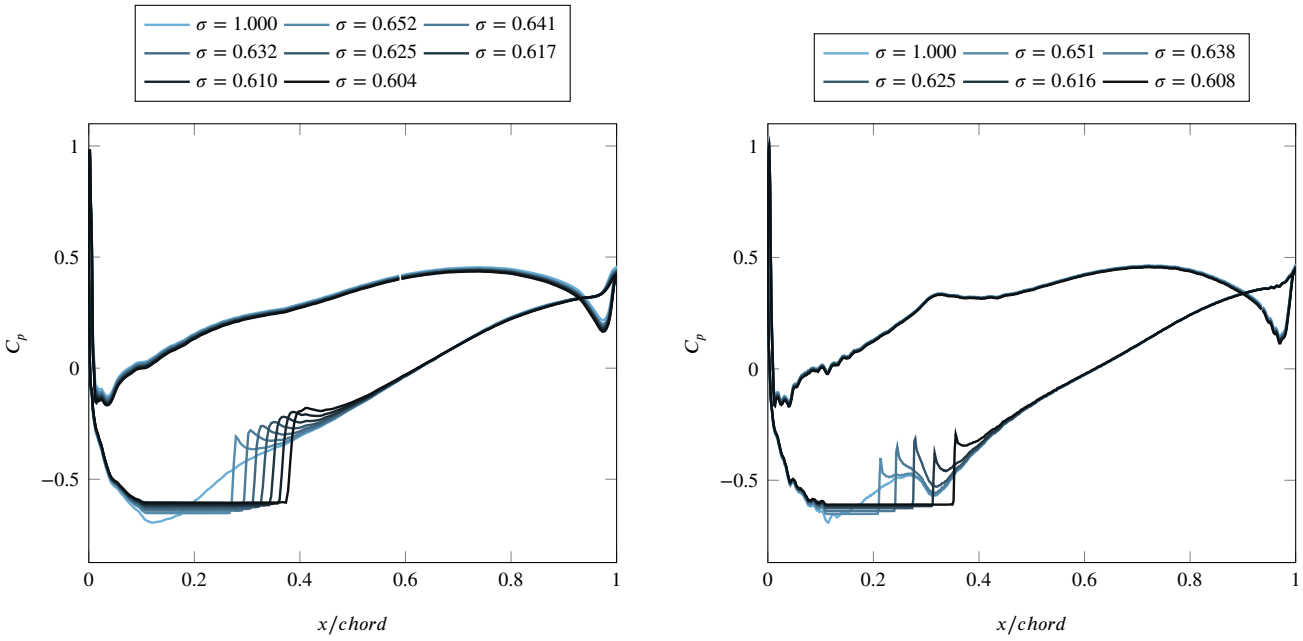

(a) Baseline (b) Design

FIGURE 15 Verification of surface pressure coefficients for both Baseline (15 a) and Design (15 b) cases at descending cavitation numbers from Fluent ZGB (with $k - \varepsilon$).

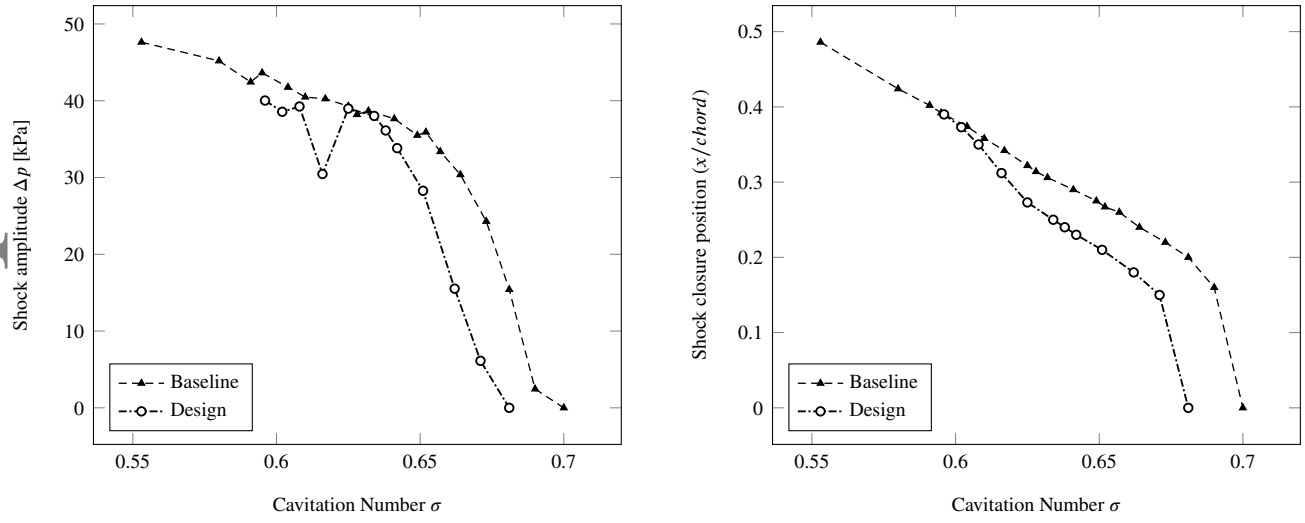

(a) Shock amplitude (b) Closure position

FIGURE 16 Closure shock progression in terms of amplitude (16 a) and location (16 b) for both Baseline and Design cases from Fluent ZGB (with $k - \varepsilon$).

5 | CONCLUSION

In the first part, the numerical techniques used to solve the cavitating flow field were detailed. Special attention was drawn to the Tohoku-Ebara barotropic state law used to model the change in mixture density, the two-dimensional preconditioning and the hypersonic multigrid method . The solver was validated using the NACA0015 hydrofoil benchmark test case.[25] Compared to the prediction delivered by Fluent with the ZGB model, our solver delivers a flow field in significantly closer agreement with the experimental results. This is most notably true for (i) the location of cavity closure and (ii) for the amplitude of the

pressure jump. The first significant conclusion drawn from this work is that the Tohoku-Ebara model constitutes an alternative for predicting cavitating flow.

In the second part, we sought to demonstrate the effectiveness of our methodology for manipulating the pressure profile at cavity closure. The algorithmic components of the inverse design procedure were laid out and tested for the described cascade geometry. A more robust permeable wall boundary was introduced with a formulation based on the acoustic propagation of the prescribed pressure. Our attempt, which consisted in imposing a shock-less loading profile, was highly successful: the target and result Δp profiles matched closely and a significant reduction in the amplitude and gradient of the closure jump was observed. Analysis of the new geometry revealed the addition of a camber kink in the closure region and highlighted its role in enforcing a smooth pressure jump.

The motivation for developing a strategy to manipulate the pressure profile in cavitating conditions was to produce less erosive blade geometries. Comparative assessments of the erosion aggressiveness for the two geometries are, therefore, currently being carried out both numerically and experimentally. The results from this analysis are to be presented shortly. The next step in the advancement of the method concerns extending the its capacity to 3D rotating flows such that cavitation in industrial applications, i.e. impellers, turbines runners and propellers, can be addressed.

5.1 | Acknowledgements

This work was funded by Ebara Corporation, Japan.

References

[1] Gulich JF. *Centrifugal Pumps*. Heidelberg: Springer. second edition ed. 2010. ISBN 978-3-642-12823-3

[2] Yu F, Zhang L, Zeng Y, Luo Z. Preliminary discussion for improving cavitating flow around hydrofoil by punching. *Procedia Engineering* 2012; 31: 261–266. doi: 10.1016/j.proeng.2012.01.1022

[3] Hofmann M, Stoffel B, Friedrichs J, Kosyna G. Similarities and Geometrical Effects on Rotating Cavitation in Two Scaled Centrifugal Pumps. In: Fourth International Symposium on Cavitation, Pasadena, CA USA. ; 2001.

[4] Sun H. Numerical study of hydrofoil geometry effect on cavitating flow. *Journal of Mechanical Science and Technology* 2012; 26(8): 2535–2545. doi: 10.1007/s12206-012-0633-y

[5] Avellan F, Dupont P. Cavitation erosion of the hydraulic machines: generation and dynamics of erosive cavities. *Proceedings of the 14th IAHR Symposium on Hydraulic Machinery: Progress within Large and High Specific Energy Units* 1988; 2: 725–738.

[6] Chan WK. Correlation between cavitation type and cavitation erosion in centrifugal pumps. *International Journal of Heat and Fluid Flow* 1990; 11(3): 269–271. doi: 10.1016/0142-727X(90)90048-G

[7] Dular M, Bachert B, Stoffel B, Širok B. Relationship between cavitation structures and cavitation damage. *Wear* 2004; 257(11): 1176–1184. doi: 10.1016/j.wear.2004.08.004

[8] Petkovšek M, Dular M. Simultaneous observation of cavitation structures and cavitation erosion. *Wear* 2013; 300(1-2): 55–64. doi: 10.1016/j.wear.2013.01.106

[9] Brennen CE. *Cavitation and bubble dynamics*. Cavitation and Bubble DynamicsNew York: Oxford University Press. oxford eng ed. 2013. ISBN 0-19-509409-3

[10] Hammitt FG. Observations on Cavitation Damage in a Flowing System. *Journal of Basic Engineering* 1963; 85(3): 347. doi: 10.1115/1.3656601

[11] Zangeneh M, Goto A, Takemura T. Suppression of Secondary Flows in a Mixed-Flow Pump Impeller by Application of Three-Dimensional Inverse Design Method: Part 1—Design and Numerical Validation. *Journal of Turbomachinery* 1996; 118(3): 536. doi: 10.1115/1.2836700

[12] Bonaiuti D, Zangeneh M, Aartojarvi R, Eriksson J. Parametric Design of a Waterjet Pump by Means of Inverse Design, CFD Calculations and Experimental Analyses. *Journal of Fluids Engineering* 2010; 132(3): 031104. doi: 10.1115/1.4001005

[13] Tiow WT, Yiu KF, Zangeneh M. Application of simulated annealing to inverse design of transonic turbomachinery cascades. *Proceedings of the Institution of Mechanical Engineers, Part A: Journal of Power and Energy* 2002; 216(1): 59–74. doi: 10.1243/095765002760024845

[14] Schmidt SJ, Sezal IH, Schnerr GH. Compressible Simulation of High-Speed Hydrodynamics with Phase Change. In: European Conference on Computational Fluid Dynamics. ; 2006; Delft, Netherlands: 1–20.

[15] Schnerr GH, Sezal IH, Schmidt SJ. Numerical investigation of three-dimensional cloud cavitation with special emphasis on collapse induced shock dynamics. *Physics of Fluids* 2008; 040703(April 2008). doi: 10.1063/1.2911039

[16] Mihatsch MS, Schmidt SJ, Adams NA. Cavitation erosion prediction based on analysis of flow dynamics and impact load spectra. *Physics of Fluids* 2015; 27(10). doi: 10.1063/1.4932175

[17] Kubota A, Kato H, Yamaguchi H. A new modelling of cavitating flows: A numerical study of unsteady cavitation on a hydrofoil section. *Journal of Fluid Mechanics* 1992; 240(3): 59–96. doi: 10.1017/S002211209200003X

[18] Zwart PJ, Gerber AG, Belamri T. A Two-Phase Flow Model for Predicting Cavitation Dynamics. In: 5th International Conference on Multiphase Flow. ; 2004.

[19] Singhal AK, Athavale MM, Li H, Jiang Y. Mathematical Basis and Validation of the Full Cavitation Model. *Journal of Fluids Engineering* 2002; 124(3): 617. doi: 10.1115/1.1486223

[20] Merkle CL, Feng J, Buelow PEO. Computational modeling of the dynamics of sheet cavitation. In: 3rd International Symposium on Cavitation. ; 1998; Grenoble, France: 47–54.

[21] Kunz RF, Boger DA, Stinebring DR, et al. A preconditioned Navier-Stokes method for two-phase flows with application to cavitation prediction. *Computers and Fluids* 2000; 29(8): 849–875. doi: 10.1016/S0045-7930(99)00039-0

[22] Delannoy Y, Kueny JL. Two-Phase Flow Approach in Unsteady Cavitation Modelling. In: Spring Meeting of the Fluids Engineering Division. ; 1990.

[23] Iga Y, Nohmi M, Goto A. Numerical Study of Sheet Cavitation Break-Off. In: Fourth International Symposium on Cavitation. ; 2001; Pasadena, CA, USA.

[24] Nohmi M, Goto A, Iga Y, Ikohagi T. Cavitation CFD in a Centrifugal Pump. In: Fifth International Symposium on Cavitation. ; 2003; Osaka.

[25] Kato C. Industry-University Collaborative Project on Numerical Predictions of Cavitating Flows in Hydraulic Machinery - Part 1: Benchmark test on cavitating hydrofoils. In: ASME-JSME-KSME Joint FLuids Engineering Conference. ; 2011

[26] Schmidt SJ, Thalhamer M, Schnerr GH. Inertia Controlled Instability and Small Scale Structures of Sheet and Cloud Cavitation. In: 7th International Symposium on Cavitation. ; 2009; Ann Arbor, Michigan, USA: 1–14.

[27] Shima E, Kitamura K. Parameter-Free Simple Low-Dissipation AUSM-Family Scheme for All Speeds. *AIAA Journal* 2012; 49(8): 1693–1709. doi: 10.2514/1.j050905

[28] Weiss JM, Smith WA. Preconditioning applied to variable and constant density flows. *AIAA Journal* 1995; 33(11): 2050–2057. doi: 10.2514/3.12946

[29] Turkel E. Preconditioned methods for solving the incompressible and low speed compressible equations. *Journal of Computational Physics* 1987; 72(2): 277–298. doi: 10.1016/0021-9991(87)90084-2

[30] Tai CH, Sheu JH, Leer vB. Optimal multistage schemes for Euler equations with residual smoothing. *AIAA Journal* 1995; 33(6): 1008–1016. doi: 10.2514/3.12860

[31] Iga Y, Shin BR, Ikohagi T, Nohmi M, Goto A. Numerical Study of Sheet Cavitation Breakoff Phenomenon on a Cascade Hydrofoil. *Journal of Fluids Engineering* 2003; 125(4): 643. doi: 10.1115/1.1596239

[32] Hayward ATJ. Compressibility equations for liquids: a comparative study. *British Journal of Applied Physics* 1967; 18(7): 965–977. doi: 10.1088/0508-3443/18/7/312

[33] Grasso F, Marini M. Solutions of hypersonic viscous flows with total variation diminishing multigrid techniques. *Computers and Fluids* 1995; 24(5): 571–592. doi: 10.1016/0045-7930(95)00009-2

[34] Blazek J, Rossow CC, Kroll N, Swanson R. A comparison of several implicit residual smoothing methods in combination with multigrid. In: 13th International Conference on Numerical Methods in Fluid Dynamics. 1993

[35] Radespiel R, Swanson RC. Progress with multigrid schemes for hypersonic flow problems. *Journal of Computational Physics* 1995; 116(1): 103–122. doi: 10.1006/jcph.1995.1009

[36] Choi YH, Merkle CL. Time-derivative preconditioning for viscous flows. *22nd Fluid Dynamics, Plasma Dynamics and Lasers Conference* 2013: 14. doi: 10.2514/6.1991-1652

[37] Meauzé G. An Inverse Time Marching Method for the Definition of Cascade Geometry. *Journal of Engineering for Power* 1982; 104(3): 650. doi: 10.1115/1.3227328

[38] Zannetti L. Time-Dependent Method to Solve the Inverse Problem for Internal Flows. *AIAA Journal* 1979; 18(7): 754–758. doi: 10.2514/3.50816

[39] Léonard O, Van den Braembussche RA. Design Method for Subsonic and Transonic Cascade With Prescribed Mach Number Distribution. In: No. 3 in International Gas Turbine and Aeroengine Congress and Exposition. ASME; 1991

[40] Hawthorne WR, Wang C, Tan CS, McCune JE. Theory of Blade Design for Large Deflections: Part I—Two-Dimensional Cascade. *Journal of Engineering for Gas Turbines and Power* 1984; 106(2): 346. doi: 10.1115/1.3239571

[41] Dang T, Damle S, Qiu X. Euler-Based Inverse Method for Turbomachine Blades, Part 2: Three-Dimensional Flows. *AIAA Journal* 2000; 38(11): 2007–2013. doi: 10.2514/2.879

[42] Demeulenaere A, Léonard O, Van Den Braembussche R. A two-dimensional Navier-Stokes inverse solver for compressor and turbine blade design. In: Proceedings of the Institution of Mechanical Engineers, Part A: Journal of Power and Energy. ; 1997